Analytical Modeling of Multi-DOF Permanent Magnet Linear Braking via Equivalent Circuit Method

Libin Cui, Guangtong Ma, *Senior Member, IEEE*, Pedram Asef, *Senior Member, IEEE*, Zhenhua Su, Piji Feng, Guanglai Huang, Shuai Xu, *Member, IEEE*, and Jun Luo, *Member, IEEE*

***Abstract*—The permanent magnet linear braking (PMLB) has garnered significant attention for its contactless operation and high force density. However, conventional analytical models often exhibit limited accuracy due to oversimplified geometric assumptions and the inability to accommodate the multi degree-of-freedom (DOF) attitude variations of the mover. To address these limitations, this paper presents a novel three-dimensional analytical model based on an equivalent circuit method. Specifically, the permanent magnet (PM) is equivalently represented as a rectangular current carrying coil using the surface current method. The mutual inductance between this equivalent PM coil and the brake coil is calculated via the discrete Neumann formula. A dynamic equivalent circuit is then constructed to determine the induced currents in the brake coil, and the resulting braking force is evaluated using both the energy method and the method of images. The proposed model is thoroughly validated through finite element method (FEM) simulations. Additionally, the impact of various attitude conditions on braking performance is systematically analyzed. Finally, experimental results obtained from a full-scale prototype and measurement system show excellent agreement with the theoretical predictions, thereby confirming the model's accuracy and practical applicability.**

***Index Terms*—permanent magnet linear braking, multi degree-of-freedom, equivalent circuit, induced current.**

I. INTRODUCTION

THE permanent magnet linear braking (PMLB) utilize electromagnetic induction principles to generate braking force without physical contact. These systems consist of a moving primary component equipped with permanent magnets (PMs) and a stationary conductive secondary component. When relative motion occurs, the varying magnetic field induces eddy currents in the secondary, producing a braking effect that opposes the motion [1-2]. Compared to conventional friction brakes, PMLBs significantly reduce mechanical wear and simplify system architecture while improving operational reliability [3]. The magnetic field provided by the PMs eliminates the need for external excitation windings, further enhancing system integration and energy efficiency [4]. These advantages make PMLBs particularly suitable for high-performance applications such as unmanned aerial vehicle (UAV) electromagnetic launch and braking systems [5].

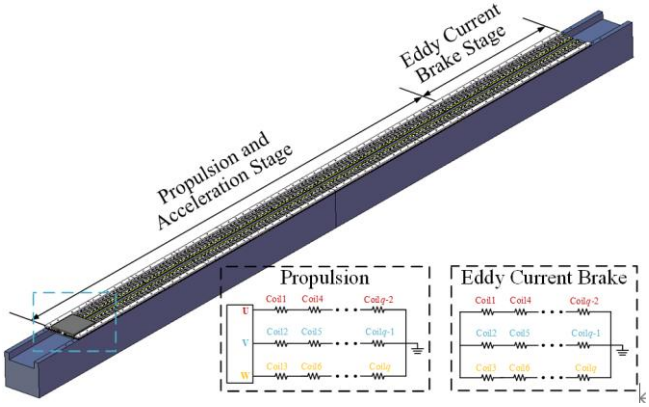

Fig. 1. Entire process of UAV electromagnetic launch system.

The secondary component in PMLBs is commonly fabricated from conductive materials such as copper, aluminum, or iron, each offering distinct performance benefits across various operational speed ranges [6-7]. To overcome the limitations inherent to single material secondaries, Cho *et al*. proposed composite a two-layer structures. However, these designs often entail increased structural complexity and exhibit limited adaptability to varying speeds [8]. In response, Kou *et al*. developed a cage-type secondary structure that dynamically adjusts its parameters to ensure a stable and high braking force over a broad speed spectrum [9]. Notably, coil-type secondary

This work was supported in part by the National Natural Science Foundation of China under Grant 52577070 and Grant 52377068, in part by the Doctoral Innovation Fund Program of Southwest Jiaotong University under Grant CX2025YB29, and in part by the Postdoctoral Fellowship Program and China Postdoctoral Science Foundation under Grant BX20250418. (*Corresponding author: Jun Luo*).

Libin Cui, Piji Feng, Guanglai Huang, Shuai Xu and Jun Luo are with the State Key Laboratory of Rail Transit Vehicle System, Southwest Jiaotong University, Chengdu 610031, China. (e-mail: cuilibin@my.swjtu.edu.cn; fpj27@my.swjtu.edu.cn; glh@my.swjtu.edu.cn; sxu@swjtu.edu.cn; jluo@swjtu.edu.cn).

Guangtong Ma is with the State Key Laboratory of Rail Transit Vehicle System, School of Electrical Engineering, Southwest Jiaotong University, Chengdu 610031, China. (e-mail: gtma@swjtu.edu.cn).

Pedram Asef is with the e-Motion and Advanced Propulsion Laboratories, Mechanical Engineering Department, University College London, London E20 3BS, United Kingdom. (e-mail: pedram.asef@ucl.ac.uk).

Zhenhua Su is with the School of Electrical Engineering, Southwest Jiaotong University, Chengdu 610031, China. (e-mail: ja5ue@my.swjtu.edu.cn).

structures offer exceptional design flexibility and adaptability. This is particularly advantageous in integrated electromagnetic launch systems for UAVs, where the same coil configuration can be seamlessly employed for both propulsion and braking as shown in Fig. 1. By modifying the electrical interconnections or circuit topology, these coil-based secondaries can be seamlessly switched between launch acceleration and braking modes, enabling compact, lightweight, and efficient dual-function system architectures.

Accurate prediction of electromagnetic braking force is crucial for achieving reliable performance and optimal design in PMLB systems. Two primary modeling techniques are commonly employed: the finite element method (FEM) and analytical approaches, each offering specific strengths and drawbacks. FEM excels at capturing intricate three-dimensional geometries and modeling nonlinear magnetic phenomena [11-13]. Nevertheless, its substantial computational requirements, sensitivity to mesh quality, and extended simulation durations diminish its practicality for iterative design and optimization processes.

In comparison, analytical models offer significantly faster computation and provide clearer physical insight, which makes them advantageous for parametric analysis and early-stage design. Nevertheless, their accuracy is often affected by simplifying assumptions, such as linear magnetic material properties, idealized geometrical representations, and approximated magnetic field distributions. Most traditional analytical models are developed in two-dimensional space, typically using the vector magnetic potential formulation [14-16]. These formulations usually assume infinitely long structures, uniform air gaps, and linear magnetic materials, which neglect transverse leakage flux, longitudinal end effects, and magnetic saturation. As a result, they are mainly suitable for systems with a single degree of freedom (DOF) and cannot accurately capture the complex spatial coupling and electromagnetic interactions that occur when translational and rotational motions coexist. To address these limitations, several improved analytical techniques have been reported. For instance, Niu *et al*. developed an iterative method that partially considers magnetic nonlinearity and introduces correction coefficients to estimate transverse end effects [17]. However, this quasi-three-dimensional formulation still relies on simplified geometric assumptions and overlooks the detailed extension of coil windings beyond the iron core. Jin *et al*. further refined analytical modeling by applying a subdomain method combined with a least-squares technique, enabling accurate treatment of slotted conductor disks, magnetic core saturation, and realistic eddy current paths [18]. Yet, their model does not accommodate systems with multi degree-of-freedom (DOF) motion, where the moving part exhibits both translational and rotational dynamics. Gulec *et al*. presented a quasi-three-dimensional reluctance network model that includes part of the geometric complexity [19], but the simplified flux-path assumptions prevent it from fully capturing the magnetic field variations and coupling effects induced by multi-DOF motion.

To overcome these limitations, this paper introduces a novel three-dimensional analytical model based on an equivalent circuit approach. The model precisely captures the complex geometries of both the coils and PMs, incorporates both transverse and longitudinal end effects, and accounts for magnetic nonlinearity. Importantly, it explicitly considers the multi-DOF motion of the moving assembly, enabling accurate and dynamic evaluation of braking performance under realistic operational conditions. The remainder of this paper is organized as follows. Section II presents a detailed description of the structure and operating principles of the PMLB. Section III outlines the development of the proposed three-dimensional analytical model. In Section IV, the model's validity is evaluated through comprehensive comparisons with FEM simulations, and the braking characteristics under various operational scenarios are analyzed. Section V describes the construction of a full-scale experimental platform for braking tests, providing empirical verification of the analytical predictions. Finally, Section VI summarizes the key findings and concludes the paper.

II. Structure and Principle

A. Structure

As illustrated in Fig. 2, the PMLB adopts a configuration with two continuous double-layer brake coils symmetrically arranged on both sides of the guideway, encasing a centrally placed I-beam-shaped mover. Mounted on the mover are four Halbach PM arrays, firmly fixed to its frame. These arrays are positioned on either side of the coils that promotes strong magnetic coupling between the PM flux and the coils. This arrangement ensures a more uniform magnetic field distribution, which enhances the induction of eddy currents within the coils. When the mover travels along the track, the relative motion between the magnets and coils induces eddy currents, and the resulting Lorentz forces resist the mover's motion, thereby providing the braking effect. With consistent flux interaction and efficient use of space, this design markedly improves braking performance and system efficiency.

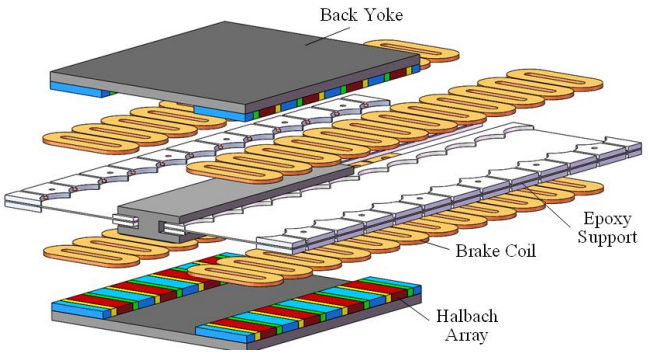

Fig. 2. Structure schematic of PMLB.

B. Principle

The PMLB operates on the principle of electromagnetic induction, which is comparable to the working mechanism of a linear induction motor. As illustrated in Fig. 3, the permanent

magnets act as the primary source and the brake coils embedded in the track serve as the secondary component. When the mover carrying Halbach permanent magnet arrays travels relative to the stationary coils, the magnetic field generated by the magnets cuts through the coils and induces eddy currents. These currents subsequently generate a secondary magnetic field that interacts with the original field of the magnets, producing Lorentz forces that oppose the motion of the mover and generate the braking effect.

The brake coils are arranged in three phases named A, B and C. Within each phase, the coils are connected in series to maintain consistent current conduction. The three phases are then connected in parallel and configured in a star connection with grounding at the neutral point. This electrical topology ensures proper management of induced currents, improves the efficiency of energy conversion and provides stable braking performance.

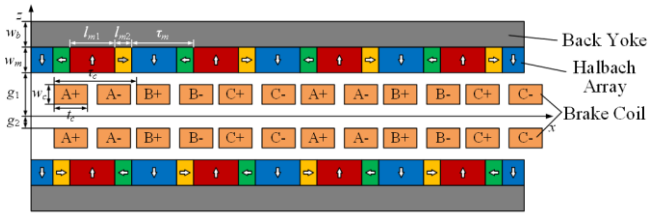

Fig. 3. Structure schematic of PMLB.

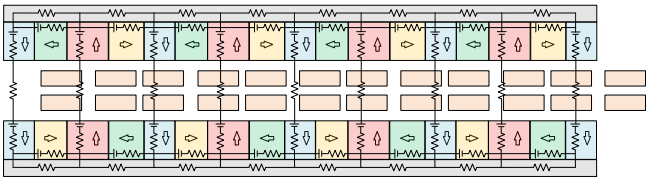

Fig. 4. Magnetic circuit diagrams of PMLB.

III. Analytical Model of PMLB

A. Spatial Coordinate

As shown in Fig. 4, the surface current method [20] enables the representation of a PM using an equivalent rectangular coil. In this approach, the surface of the PM is treated as a distribution of surface currents, and it avoids the complexity of solving for the volume current distribution within the magnet itself. Thus, the thickness of the PM equivalent coil is zero and not need to be discretized.

A coordinating system is set up to describe the magnet's position and orientation in the system. As plotted in Fig. 5, the PM equivalent coil is discretized into n_{m1}, n_{m2}, and N_m segments in the length, height, and width directions, respectively. For each discrete unit, the local coordinate matrix is derived in (1), where l_m and h_m represent the length and height of the equivalent coil, and i_m represents the i_m-*th* discrete segment along the centerline. Additionally, the discretization interval in the width direction of the section Δy_m in (1) is calculated as follows,

$$\Delta y_m(j_m)=\frac{(2j_m-N_m-1)w_m}{2N_m}, \tag{2}$$

where j_m denotes the j_m-*th* discrete segment, and w_m represents the width of the equivalent coil.

$$A_m(i_m)=\begin{cases}\left[-\frac{l_m}{2}+\frac{l_m(i_m-1)}{n_{m1}} \quad \Delta y_m \quad -\frac{h_m}{2}\right], & 0<i_m\le n_{m1}\\ \left[\frac{l_m}{2} \quad \Delta y_m \quad -\frac{h_m}{2}+\frac{h_m(i_m-n_{m1}-1)}{n_{m2}}\right], & n_{m1}<i_m\le n_{m1}+n_{m2}\\ \left[\frac{l_m}{2}-\frac{l_m(i_m-n_{m1}-n_{m2}-1)}{n_{m1}} \quad \Delta y_m \quad \frac{h_m}{2}\right], & n_{m1}+n_{m2}<i_m\le 2n_{m1}+n_{m2}\\ \left[-\frac{l_m}{2} \quad \Delta y_m \quad \frac{h_m}{2}-\frac{h_m(i_m-2n_{m1}-n_{m2}-1)}{n_{m2}}\right], & 2n_{m1}+n_{m2}<i_m\le 2n_{m1}+2n_{m2}\end{cases}. \tag{1}$$

$$A_c(i_c)=\begin{cases}\left[-\frac{L_c}{2}+r_c\cos\left[\frac{\pi}{2}\left(\frac{i_c-1}{n_{c1}}-1\right)\right] \quad \Delta y_c \quad -\frac{H_c}{2}+r_c-r_c\sin\left[\frac{\pi}{2}\left(\frac{i_c-1}{n_{c1}}\right)\right]\right], & 0<i_c\le n_{c1}\\ \left[r_c\cos\left[\frac{\pi}{2}\left(\frac{i_c-n_{c1}-1}{n_{c1}}-1\right)\right] \quad \Delta y_c \quad -\frac{H_c}{2}+r_c\sin\left[\frac{\pi}{2}\left(\frac{i_c-n_{c1}-1}{n_{c1}}\right)\right]\right], & n_{c1}<i_c\le 2n_{c1}\\ \left[\frac{L_c}{2} \quad \Delta y_c \quad -\frac{H_c}{2}+r_c+\frac{(H_c-2r_c)(i_c-2n_{c1}-1)}{n_{c2}}\right], & 2n_{c1}<i_c\le 2n_{c1}+n_{c2}\\ \left[\frac{L_c}{2}-r_c\cos\left[\frac{\pi}{2}\left(\frac{i_c-2n_{c1}-n_{c2}-1}{n_{c1}}-1\right)\right] \quad \Delta y_c \quad \frac{H_c}{2}-r_c+r_c\sin\left[\frac{\pi}{2}\left(\frac{i_c-2n_{c1}-n_{c2}-1}{n_{c2}}\right)\right]\right], & 2n_{c1}+n_{c2}<i_c\le 3n_{c1}+n_{c2}\\ \left[-r_c\cos\left[\frac{\pi}{2}\left(\frac{i_c-3n_{c1}-n_{c2}-1}{n_{c1}}-1\right)\right] \quad \Delta y_c \quad \frac{H_c}{2}-r_c\sin\left[\frac{\pi}{2}\left(\frac{i_c-3n_{c1}-n_{c2}-1}{n_{c1}}\right)\right]\right], & 3n_{c1}+n_{c2}<i_c\le 4n_{c1}+n_{c2}\\ \left[-\frac{L_c}{2} \quad \Delta y_c \quad \frac{H_c}{2}-r_c-\frac{(H_c-2r_c)(i_c-4n_{c1}-n_{c2}-1)}{n_{c2}}\right], & 4n_{c1}+n_{c2}<i_c\le 4n_{c1}+2n_{c2}\end{cases}. \tag{7}$$

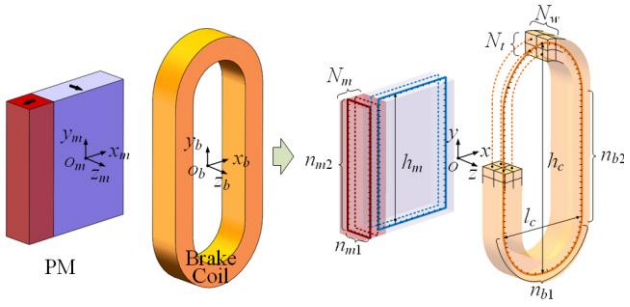

Fig. 5. Discretizing of PM equivalent coil and brake coil.

The coordinate matrix in (1) is constructed in the local coordinate system, and the spatial transformation must be applied to account for the varying position and orientation of the PM relative to the brake coils. First, the displacement matrix M_m is used to describe the translation of the magnet in space, capturing the shift in position as the magnet moves relative to the track. Second, the deflection matrix M_d is introduced for the horizontal magnetizing magnet, which accounts for the deflection direction of magnetization. Finally, the spatial attitude change matrix M_t is employed to model the variations in the magnet's orientation or tilt as it moves through space. These matrices together allow for the comprehensive modeling of the magnet's motion and its changing spatial attitude.

$$A_m^g(i_m,j_m,m,t)=A_m(i_m,j_m)\cdot M_m\cdot M_d\cdot M_t. \tag{3}$$

$$M_m=\begin{bmatrix}1 & 0 & 0 & 0\\ 0 & 1 & 0 & 0\\ 0 & 0 & 1 & 0\\ \frac{(m-1)\tau_m}{2} & \frac{w_m}{2}+g_1 & 0 & 1\end{bmatrix}. \tag{4}$$

$$M_d=\begin{bmatrix}\cos 90^\circ & \sin 90^\circ & 0 & 0\\ -\sin 90^\circ & \cos 90^\circ & 0 & 0\\ 0 & 0 & 1 & 0\\ 0 & 0 & 0 & 1\end{bmatrix},\quad m=2u\ \ (u=1,2,\ldots). \tag{5}$$

$$M_t=\begin{bmatrix}1 & 0 & 0 & 0\\ 0 & \cos\psi_x & \sin\psi_x & 0\\ 0 & -\sin\psi_x & \cos\psi_x & 0\\ 0 & 0 & 0 & 1\end{bmatrix}\begin{bmatrix}\cos\psi_y & 0 & -\sin\psi_y & 0\\ 0 & 1 & 0 & 0\\ \sin\psi_y & 0 & \cos\psi_y & 0\\ 0 & 0 & 0 & 1\end{bmatrix}\begin{bmatrix}\cos\psi_z & \sin\psi_z & 0 & 0\\ -\sin\psi_z & \cos\psi_z & 0 & 0\\ 0 & 0 & 1 & 0\\ 0 & 0 & 0 & 1\end{bmatrix}\begin{bmatrix}0 & 0 & 0 & 0\\ 0 & 0 & 0 & 0\\ 0 & 0 & 0 & 0\\ v_x\cdot t & \Delta y & \Delta z & 1\end{bmatrix}. \tag{6}$$

Where m represents the m-th number of PM, τ_m denotes pitch of the PM, g_1 shows the transverse spacing of magnets on both sides, ψ_x denotes the roll angle of the mover, ψ_y is the pitch angle of the mover, ψ_z is the yaw angle of the mover, v_x corresponds to the velocity and t represents the time.

Similarly, the discrete configuration of the brake coils is shown in Fig. 4, because the coil has thickness in the physical space, it is discretized into n_{c1}, n_{c2}, N_w and N_t segments in the arc, height, width and thickness directions, respectively. The coordinate matrix of the coil in the local coordinate system can be expressed in (7), where r_c represents the radius of fillet, and i_c shows the i_c-th discrete segment along the centerline. Due to the discretization in the width and thickness directions of the brake coil, the length l_c and height h_c are turning into L_c and H_c, and can be expressed as,

$$L_c(j_c)=l_c+\frac{(2j_c-N_t-1)t_c}{N_t}, \tag{8}$$

$$H_c(j_c)=h_c+\frac{(2j_c-N_t-1)t_c}{N_t}, \tag{9}$$

where j_c denotes the j_c-th discrete segment, and t_c represents the thickness of the brake coil.

The discrete distance in the width direction Δy_c is calculated, which defines the interval at which the coil is subdivided.

$$\Delta y_c(k_c)=\frac{(2k_c-N_w-1)w_c}{2N_w}. \tag{10}$$

Where k_c denotes the k_c-th discrete segment, and w_c represents the width of the brake coil.

The spatial transformation also needs to be applied to the brake coil to ensure a coherent representation of the system's spatial positioning. In this case, only a single spatial transformation matrix M_c is required for the brake coil, which accounts for its position and orientation in space relative to the PM and the track.

$$A_c^g(i_c,j_c,k_c,n)=A_c(i_c,j_c,k_c)\begin{bmatrix}1 & 0 & 0 & 0\\ 0 & 1 & 0 & 0\\ 0 & 0 & 1 & 0\\ \frac{(n-1)\tau_c}{2} & \frac{w_c+g_2}{2} & 0 & 1\end{bmatrix}. \tag{11}$$

Where n represents the n-th number of brake coil, τ_c denotes the pitch of the brake coil, g_2 is the transverse spacing of coils on both sides.

B. Equivalent Circuit

Base on the discrete Neumann formula [21], the mutual inductance of each discrete element is computed as described in Fig. 6, and the total mutual inductance between the i-th brake coil and the j-th PM can be determined by summing them up as follows,

$$M_{i,j}=\frac{\mu_0 N_1 N_2}{4\pi N_w N_t N_m}\sum_{i_c=1}^{n_c}\sum_{j_c=1}^{N_t}\sum_{k_c=1}^{N_w}\sum_{i_m=1}^{n_m}\sum_{j_m=1}^{N_m}\left(\frac{A_c^g\cdot A_m^g}{\left|A_c^g-A_m^g\right|}\right), \tag{12}$$

where N_1 and N_2 represent the turns of brake coil and PM equivalent coil, and μ_0 is the air magnetic permeability.

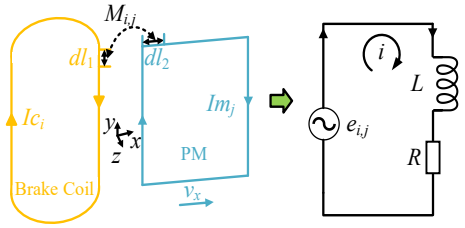

Fig. 6. Equivalent circuit of a single brake coil and single PM.

As the primary PM sweeps across the secondary windings, the time-varying magnetic flux linking the coils induces a current, as illustrated in Fig. 5. Following Faraday's law [22], the induced electromotive force (EMF) in each winding can be expressed as,

$$e_{i,j} = -N_i \frac{d\phi_{i,j}}{dt} = -\frac{d(M_{i,j} Im_j)}{d(x/v_x)} = -Im_j v_x \frac{\partial M_{i,j}}{\partial x} , \quad (13)$$

where I_m is the surface current of PM and can be calculated as,

$$I_m = M \cdot w_m / N_2 , \quad (14)$$

where the M is the coercive force of PM.

During practical operation, it is common for m PMs to simultaneously interact with n brake coils. To rigorously capture the collective effects and mutual interactions between the PMs of the mover and the entire set of track coils, a fully coupled equivalent circuit is established, as depicted in Fig. 7. The blue dashed box represents the single PM and single coil loop as shown in Fig. 5. According to Kirchhoff's voltage law, the equivalent circuit equation can be established as follows,

$$\begin{cases} \sum_{i=1}^{n/6}[(R_{3i-2}+R_{3i-1})i_1 + (L_{3i-2}+L_{3i-1})\frac{di_1}{dt}] = \sum_{i=1}^{n/6}\sum_{j=1}^{m}(e_{3i-2,j} - e_{3i-1,j}) \\ \sum_{i=1}^{n/6}[(R_{3i-1}+R_{3i})i_2 + (L_{3i-1}+L_{3i})\frac{di_2}{dt}] = \sum_{i=1}^{n/6}\sum_{j=1}^{m}(e_{3i-1,j} - e_{3i,j}) \end{cases} , \quad (15)$$

where R represents the resistance of the brake coil, i_1 and i_2 are the upper and lower circuit loop currents, L is the inductance of the coil and can be calculated as,

$$L_i = \sum_{j=1}^{m} M_{i,j} \cdot \quad (16)$$

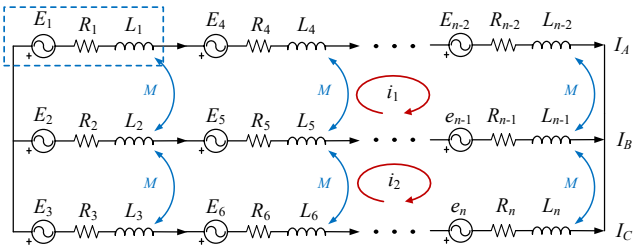

Fig. 7. Fully coupled dynamic equivalent circuit.

In the process of calculating the loop currents i_1 and i_2 in the circuit, an iterative method was employed. The continuous motion was discretized so that the current at each new time step could be expressed as a function of the current at the previous step, as shown in equation (17). Substituting equation (17) into equation (15) yielded the analytical forms of i_1 and i_2. To initiate the iteration, an initial value was assigned to the current at the starting time. The motion of the permanent magnet in the dynamic circuit led to changes in the inductance parameters, which had a significant impact on the evolution of the loop currents. At each iteration, the inductance values were updated, allowing the current calculations to progressively approach greater accuracy. This iterative procedure effectively captured the transient characteristics of the circuit by reflecting the time-varying inductance caused by the PM's movement. After sufficient time steps, the computed values of i_1 and i_2 converged to their true states, representing the actual operating conditions of the system.

$$i = i(t-\Delta t) + \frac{di}{dt}\Delta t \cdot \quad (17)$$

However, it should be noted that i_1 and i_2 do not directly represent the actual currents in the brake coil. As illustrated in Fig. 6, the brake coil is divided into A, B, and C three groups. The relationship between the true currents in these groups and the loop currents is further detailed as follows,

$$I_c(n,t) = \begin{cases} i_1(t), & n = 3u-2 \quad (u = 1,2,...) \\ -i_1(t) + i_2(t), & n = 3u-1 \quad (u = 1,2,...) \\ -i_2(t), & n = 3u \quad (u = 1,2,...) \end{cases} \cdot \quad (18)$$

C. Method of Image

The insertion of mover PMs between magnetic yokes significantly distorts the magnetic field, preventing it from following the ideal free-space distribution. At the PM–yoke interface, the discontinuity in magnetomotive force relative to the interior of the PMs is equivalent to the presence of surface currents. This phenomenon introduces additional complexity into the modeling and evaluation of the field. To overcome this difficulty, the influence of the yokes is usually represented through the method of images [23-24]. Fig. 8 provides a schematic representation of this principle, the physical yokes are mathematically substituted by an infinite set of virtual sources, leaving only the PMs and their image counterparts to define the magnetic environment.

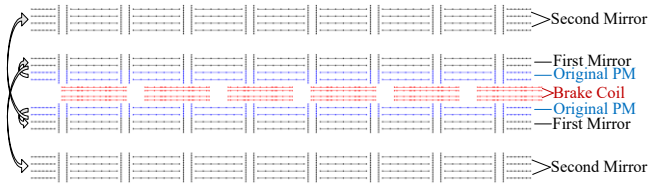

Fig. 8. Method of Image.

Finally, the energy method [25] is used to solve the braking electromagnetic force of the PMLB, and the electromagnetic force in the x direction is equal to the partial derivative of the total energy of the system in this direction.

$$F_x(t) = \sum_{m=1}^{q}\sum_{n=1}^{p} I_m(m,t) \cdot \frac{\partial M_{m,c}(m,n,t)}{\partial x} \cdot I_c(n,t) \cdot \quad (19)$$

IV. Finite Element Analysis

A. FEM Model

A three-dimensional FEM model of the PMLB was constructed using MagNet to validate the proposed analytical framework, as shown in Fig. 9. The key geometric parameters are listed in Table I. Taking advantage of the structural symmetry of the system, only one side was modeled. This approach significantly reduces computational demand while preserving the essential electromagnetic characteristics of the braking.

The electrical configuration of the brake coils is also shown in Fig. 10. The entire system consists of 24 coils, which are divided into three phases labeled A, B, and C. These phases are connected in parallel. Each phase contains eight coils connected in series, enabling balanced three-phase induced currents and supporting efficient generation of electromagnetic braking force.

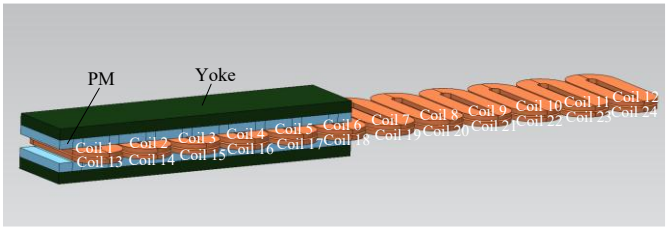

Fig. 9. Single-sided FEM model of PMLB.

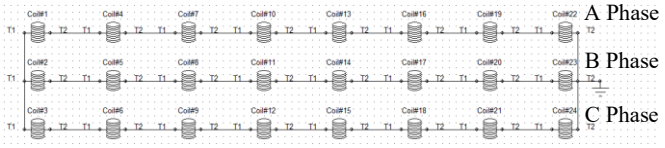

Fig. 10. Circuit connection of PMLB.

TABLE I
DESIGN PARAMETERS OF PMLB

Brake coil	Value	PM	Value
Length l_c	42 mm	Vertical magnetizing magnet length l_{m1}	40 mm
Height h_c	142 mm	Horizontal magnetizing magnet length l_{m2}	14 mm
Fillet radius r_c	21 mm	Height h_m	100 mm
Pitch τ_c	72 mm	Width w_m	12 mm
Width w_c	6 mm	Pitch τ_m	54 mm
Thickness t_c	27 mm	Yoke width w_b	15 mm
Gap g_1	9 mm	Gap g_2	2 mm
Turns N_p	22		

B. Transient braking force

Fig. 11 presents the variation of the induced currents in the brake coils at a constant speed of 1 m/s. The currents in the three phases exhibit sinusoidal waveforms with phase shifts of approximately 120 electrical degrees between them, which is consistent with the behavior of a balanced three-phase system. The peak amplitude of the induced current in each phase reaches approximately 83 A. The FEM results are in good agreement with the predictions of the proposed analytical model with an error of 1.9%, thereby confirming its validity.

It is important to note that during the initial stages of the iterative calculation, the current waveforms deviate slightly from the ideal sinusoidal shape. This deviation occurs because the induced currents are obtained through an iterative process that requires multiple steps to achieve convergence. In the early iterations, the current values are still evolving and have not yet stabilized. Nevertheless, even at these preliminary stages, the estimated current profiles show strong consistency with the FEM results.

Fig. 12 illustrates the transient braking force generated by the PMLB operating at a constant speed of 1 m/s. Once the induced currents converge through the iterative computation process, the braking forces on both sides of the system can be stabilized. The total average braking force reaches approximately 3.31 kN. The results obtained from the FEM show close agreement with those predicted by the analytical model, the further validating the accuracy and reliability of the proposed approach. To facilitate a more detailed comparison between the two methods, a zoomed-in view of selected segments of the braking force curves is provided in the figure. As shown, the maximum deviation between the analytical and FEM results is less than 2.3%. This high level of consistency confirms that the analytical model is capable of accurately capturing the transient electromagnetic behavior of the system. Specifically, the total computation time required for the analytical model is only 107 s, while the FEM simulation under the same conditions requires approximately 96 h to complete. All computations were carried out on a workstation equipped with a 3.20 GHz AMD Ryzen 7 7735H processor, Radeon Graphics, 32.0 GB RAM, and Windows 11 operating system. The detailed comparison of computation time and accuracy between the analytical model and FEM is summarized in TABLE II.

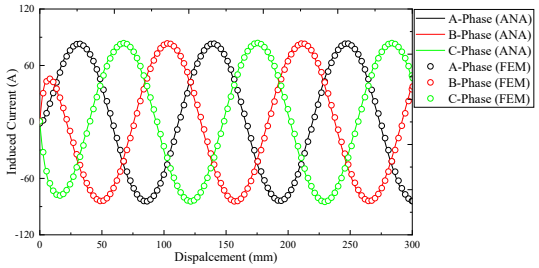

Fig. 11. Induced current in the brake coil. under a velocity of 1 m/s.

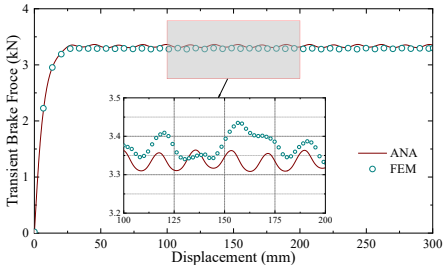

Fig. 12. Transient braking force under a velocity of 1 m/s.

TABLE II
COMPARISON OF COMPUTATION TIME AND ACCURACY

	Analytical	FEM simulations	Error
Computation time	107 s	96 h	/
Thrust result	3.31 kN	3.39 kN	2.3%

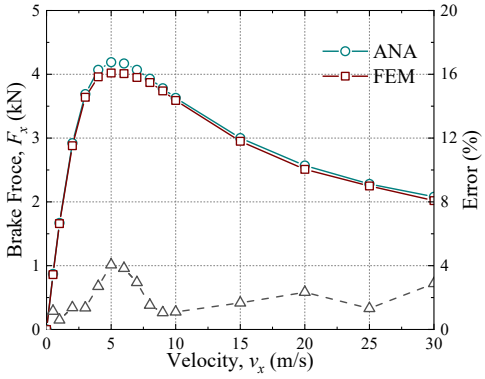

Fig. 13. Variation of the brake force with velocity.

Fig. 13 shows the variation in brake force with respect to the

relative motion speed of the PMLB. The braking force initially increases as the speed rises, reaching a peak of approximately 4.1 kN at around 5 m/s. Beyond this point, the force gradually decreases. This behavior is characteristic of braking systems where the interaction between the induced current and the changing magnetic field leads to a non-monotonic braking response. The analytical model exhibits excellent agreement with the finite element simulation results across the full speed range. This consistency remains evident even at higher speeds. As shown in Fig. 13, the maximum deviation occurs at 5 m/s and is only 4.06%, indicating that the analytical model remains highly consistent with the FEM results and accurately predicts the braking characteristics of the PMLB. These results confirm the accuracy and robustness of the proposed analytical model in predicting braking performance over a wide range of operating speeds.

V. Braking Characteristics

A. Influence of vertical displacement

In practical applications, the mover often deviates from ideal straight-line motion along the x-axis, exhibiting multi-DOF attitude variations. These include translational displacements such as vertical and horizontal shifts, and rotational deviations like pitch, roll, and yaw. As shown in Fig. 14, vertical displacement specifically refers to motion along the *z*-axis. To evaluate the effect of vertical displacement on braking performance, simulations were conducted with displacements from −2 mm to 2 mm in 0.2 mm steps. The resulting braking force, presented in Fig. 15, shows a symmetric distribution around the vertical axis and increases with displacement magnitude. This behavior is mainly due to air gap changes. As the PM assembly moves closer to one side, the reduced gap strengthens the magnetic field on that side, while the widened gap weakens it on the opposite side. Since magnetic field strength decays exponentially with distance, the net flux density increases near the narrower gap, enhancing the overall braking force.

Note that capturing non-uniform magnetic fields under spatial attitude variations requires a full 3D FEM model, which is computationally intensive, and each simulation takes about 96 hours. Thus, only the case of 1.8 mm vertical displacement was analyzed with FEM. The simulated transient braking force is approximately 3.37 kN and closely matches the analytical prediction, with a maximum deviation of 3.2%. This confirms the model's accuracy under spatial deviations.

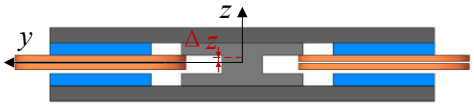

Fig. 14. Vertical displacement of PMLB.

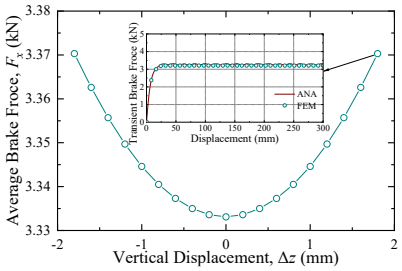

Fig. 15. Variation of braking force with vertical displacement.

B. Influence of horizontal displacement

The influence of horizontal displacement on braking performance is also investigated. As illustrated in Fig. 16, horizontal displacement refers to the lateral offset of the mover along the *y*-axis. Due to the relatively larger structural tolerance in this direction, the displacement range is extended from −10 mm to 10 mm, with a step size of 1 mm. This broader range enables a more comprehensive evaluation of braking behavior under lateral deviations.

The simulation results presented in Fig. 17 show a gradual decrease in braking force as horizontal displacement increases. This reduction is primarily caused by the increasing misalignment between the PMs and the brake coils, which weakens the magnetic coupling and reduces the induced eddy currents. Furthermore, the curved geometry of the coil edges alters the direction of the current from that of an ideal straight conductor, resulting in a redistribution of the Lorentz force. This redistribution reduces the effective braking force in the desired direction. The results also indicate that the braking force exhibits symmetry for both positive and negative displacements, consistent with the structural layout of the system. Given the high computational cost associated with three-dimensional FEM simulations, only the case corresponding to a horizontal displacement of 10 mm was selected for detailed FEM analysis. The transient braking force obtained from the FEM simulation is approximately 3.28 kN, which closely aligns with the prediction from the analytical model.

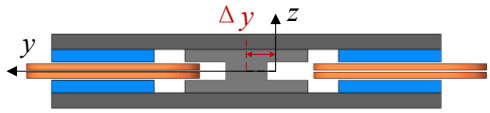

Fig. 16. Horizontal displacement of PMLB.

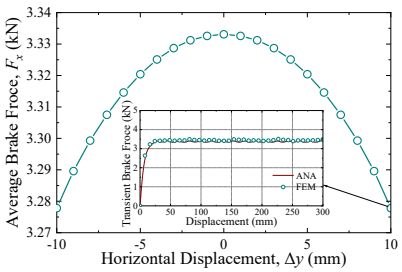

Fig. 17. Variation of braking force with horizontal displacement.

C. Influence of yaw angle

The analysis is further extended to examine the impact of angular deviations, specifically the influence of yaw angles on braking performance. As illustrated in Fig. 18, the yaw angle represents the rotation of the mover about the *z*-axis. To evaluate its effect, the yaw angle is varied from −10° to 10° in 1° increments.

Fig. 19 shows the results for a gradual decrease in brake force as the absolute value of the yaw angle increases. This decline is primarily due to geometric misalignment caused by yaw rotation. As the yaw angle increases, the ends of the PMs shift away from the brake coils, therefore weakening the effective magnetic coupling and reducing their contribution to the overall braking force. Also, the braking force profile exhibits symmetry with respect to positive and negative yaw angles, which reflects the physical symmetry of the rotational motion.

These findings highlight the sensitivity of braking performance to angular misalignment and further demonstrate the capability of the analytical model to accurately capture such effects. To support the analytical results, a full three-dimensional FEM simulation was performed for the case of a 10° yaw angle. The transient braking force obtained from the FEM model is approximately 2.72 kN, which closely agrees with the value predicted by the analytical model. This strong consistency further validates the reliability and accuracy of the proposed approach in evaluating braking performance under angular deviation conditions.

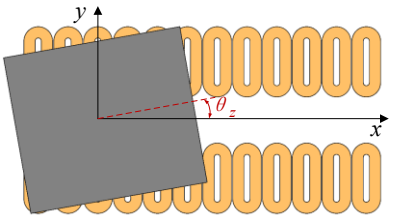

Fig. 18. Yaw angle of PMLB.

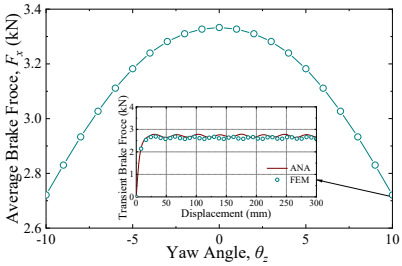

Fig. 19. Variation of braking force with yaw angle.

D. Influence of pitch angle

The analysis then proceeds to investigate the influence of the pitch angle, which represents the rotation of the mover about the *y*-axis, as illustrated in Fig. 20. Due to physical space constraints in the system, the pitch angle is evaluated within a limited range from −1° to 1°, using an increment of 0.1°. Although this range is narrower than those considered in previous angular deviation analyses, it is sufficient to capture the behavior relevant to practical operating conditions.

Fig. 21 presents that the braking force increases monotonically with the pitch angle within the examined range. This trend suggests that small angular deflections can enhance braking performance without causing significant misalignment. The improvement is primarily attributed to improved magnetic coupling between the PMs and the brake coils as the mover undergoes a slight rotational displacement with the *y*-axis. To verify the accuracy of the analytical predictions, a full three-dimensional FEM simulation was carried out for a pitch angle of 0.5°. The resulting transient braking force is approximately 3.35 kN, which closely matches the value obtained from the analytical model.

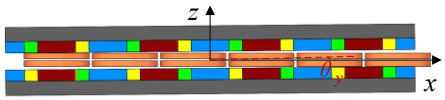

Fig. 20. Pitch angle of PMLB.

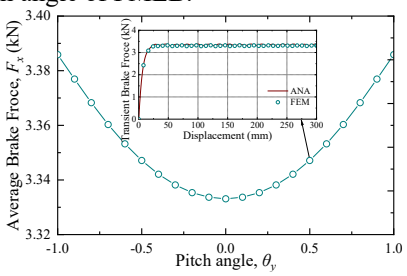

Fig. 21. Variation of braking force with pitch angle.

E. Influence of roll angle

The final parameter examined is the roll angle, which refers to the rotation of the mover about the x-axis, as illustrated in Fig. 22. Due to mechanical constraints, the analysis is restricted to a practical range from −1° to 1°, with evaluations conducted in increments of 0.1°.

As presented in Fig. 23, the brake force increases gradually with the roll angle within this range. This slight enhancement is primarily attributed to improved magnetic coupling resulting from minor changes in the spatial orientation between the PMs and the brake coils. Although the variation range is narrow, the observed trend suggests that small roll deviations can positively affect braking performance without introducing significant misalignment or system instability. To verify the analytical findings, a full three-dimensional FEM simulation was conducted for a roll angle of 0.5°. The resulting transient braking force was approximately 3.35 kN, which closely matches the prediction from the analytical model.

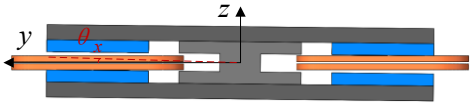

Fig. 22. Roll angle of PMLB.

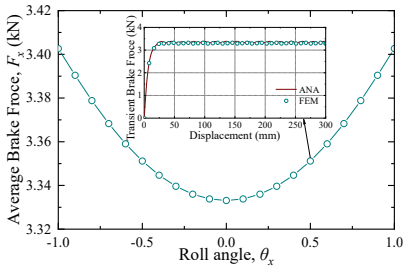

Fig. 23. Variation of braking force with roll angle.

VI. Prototype Verification

To experimentally validate the braking performance, a full-scale prototype of the PMLB was developed for use in UAV electromagnetic launch systems, as shown in Fig. 24. The prototype is installed on a high-precision granite foundation composed of two seamlessly connected 6-meter slabs. These slabs are manually leveled to ensure accurate horizontal alignment, providing a stable base for the installation of the coil arrays, as illustrated in Fig. 24 (a).

Each coil module contains 12 coils arranged in two layers, with six coils in the upper layer and six in the lower layer, as detailed in Fig. 24 (b). These modules are assembled into continuous arrays on both the left and right sides of the prototype, with a total of 26 modules per side. All modules are securely fixed to the granite base using bolts and clamping plates to ensure mechanical stability throughout operation.

Functionally, the coil array is divided into two sections. The front section is responsible for electromagnetic propulsion and acceleration, while the rear section serves as the braking zone. The mover adopts an I-beam structural configuration and integrates four Halbach PM arrays, as depicted in Fig. 24 (c). Its motion is constrained to a single axis by means of linear guide rails and precision-aligned sliding blocks, which are directly mounted on the granite foundation. This setup ensures smooth and stable translation during testing.

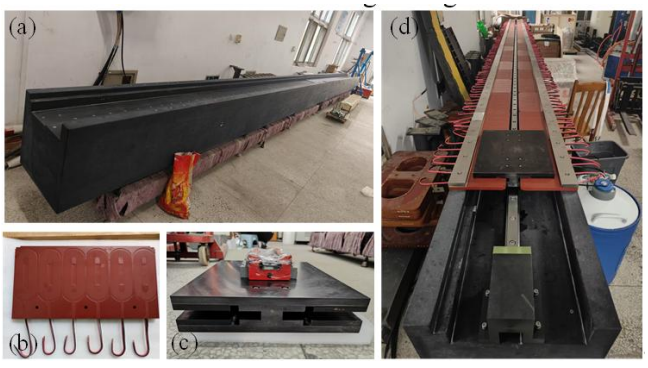

Fig. 24. Full-scale UAV electromagnetic launch platform. (a) Granite foundation. (b) Coil module. (c) Halbach PM array move. (d) PMLB prototype.

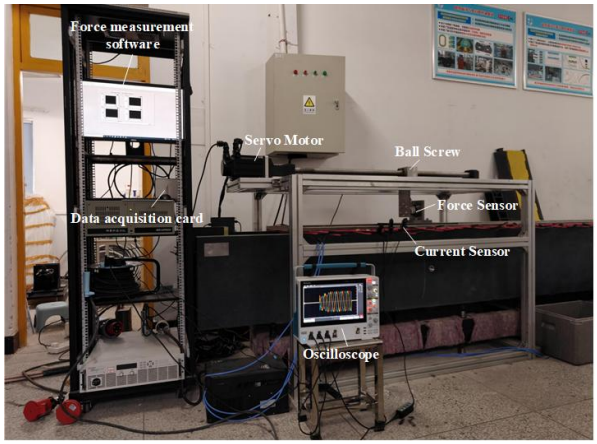

Fig. 25. PMLB dynamic measurement system.

A dedicated measurement system was developed to evaluate the dynamic performance of the PMLB, as shown in Fig. 25. The setup includes an aluminum alloy frame that supports a servo motor and a ball screw actuator. The screw nut is linked to the mover through a three-axis force sensor. During operation, the servo motor drives the screw to produce steady linear motion of the mover, while the braking force is detected by the force sensor with a 500 Hz sampling and recorded via a data acquisition card. The data are transmitted to the host computer for analysis. To monitor eddy currents in the coil array, current sensors were placed on the A, B, and C phase groups and connected to an oscilloscope with a 25 kHz sampling, which displayed the current waveforms in real time. A LabVIEW-based interface was also used to visualize and log the braking force.

In the test, the servo motor was set to a rotational speed of 1200 r/min, which was converted through the ball screw mechanism to achieve a constant linear velocity of 0.1 m/s for the mover. At this speed, the induced currents in the three-phase coils reached a peak amplitude of about 8.5 A and showed sinusoidal waveforms, as illustrated in Fig. 26. The results agreed well with both analytical predictions and FEM simulations. Small fluctuations near the current peaks were observed, likely due to mechanical vibrations of the frame and the influence of electromagnetic noise, leading to a maximum error of about 3.3%. At the same time, the braking force was measured, as shown in Fig. 27. The recorded force was around 360 N, with a maximum deviation of 5.3% compared with theoretical and simulation results. These findings verify the accuracy of the equivalent circuit method in modeling and predicting the dynamic behavior of the PMLB.

It was observed that the measured braking forces were consistently smaller than the analytical predictions, showing a negative deviation. This primarily resulted from the epoxy encapsulation of the stator coils, which increased the coil thickness from 14 mm to about 15 mm and consequently enlarged the air gap between the magnets and the coil surface, reducing the magnetic coupling strength. In addition, slight mechanical vibrations of the aluminum frame introduced minor oscillations in the force signal, especially at low velocities. Nevertheless, the total deviation remained within 5%, confirming that the analytical model accurately represents the electromagnetic behavior of the PMLB system.

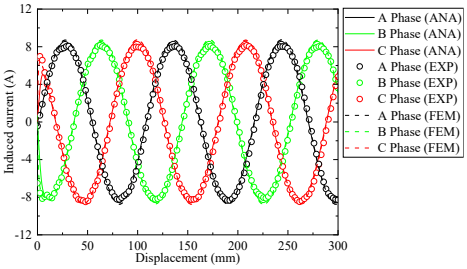

Fig. 26. Induced current under a velocity of 0.1 m/s.

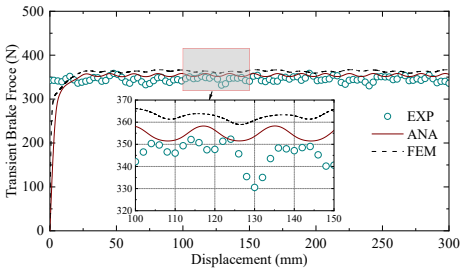

Fig. 27. Transient brake force under a velocity of 0.1 m/s.

Subsequently, the servo motor operated at a rotational speed of 2400 r/min, driving the mover to reach a constant linear velocity of 0.2 m/s. The system was tested again to measure both the induced eddy currents and the braking force, as shown in Fig. 28 and Fig. 29, respectively. The current waveforms for the A, B, and C phase coils remained sinusoidal, with the peak amplitude reaching approximately 17.1 A. While the overall waveform closely followed the expected pattern, minor irregularities were observed at the peak current values. These deviations are likely caused by mechanical vibrations in the aluminum alloy frame and resulted in a maximum measurement error of approximately 3.8%.

Under the same operating condition, the braking force was measured and found to be approximately 720 N. The experimental data again demonstrated good agreement with the predictions from both the analytical model and the finite element simulation. The maximum deviation in the measured braking force was approximately 5.4%. These results further confirm the robustness and accuracy of the proposed analytical model, which remains consistent across different operating speeds.

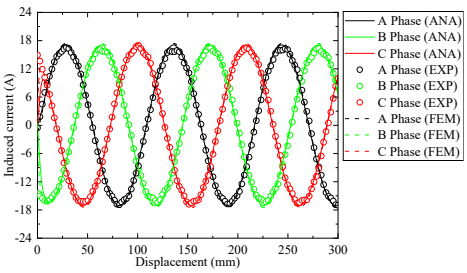

Fig. 28. Induced current under a velocity of 0.2 m/s.

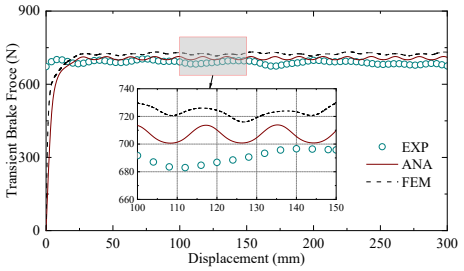

Fig. 29. Transient brake force under velocity of 0.2 m/s.

Finally, due to the speed limitation of the servo motor, which was set to a maximum rotational speed of 3600 r/min, together with the constraints of the ball screw transmission system and the measurement range of the force sensor, the maximum achievable testing velocity was limited to 0.3 m/s. At this speed, additional tests were conducted to measure both the induced eddy currents and the braking force, as shown in Fig. 30 and Fig. 31. The current waveform maintained a sinusoidal shape, with the peak amplitude increasing to approximately 25.9 A. The maximum measurement error for the current was observed to be 2.1%. The measured induced current amplitudes increased with speed, and the noise and vibration effects were proportionally more significant at lower current amplitudes, leading to more noticeable signal disturbances under low-speed conditions. Simultaneously, the braking force was measured at approximately 1080 N. This value closely matched the predictions obtained from both the analytical model and the FEM model, with a maximum deviation of about 6.7%. These results further confirm the reliability and accuracy of the proposed analytical approach.

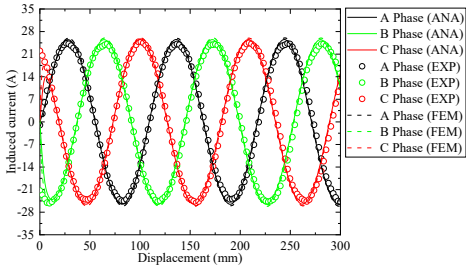

Fig. 30. Induced current under a velocity of 0.3 m/s.

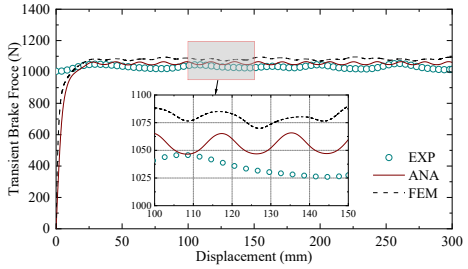

Fig. 31. Transient brake force under a velocity of 0.3 m/s.

VII. Conclusion

In this paper, a novel three-dimensional analytical model based on an equivalent circuit framework was developed to evaluate the braking performance of PMLB, with a focus on

their application in UAV electromagnetic launch systems. The model incorporates complex geometric structures and accurately accounts for multi-DOF motion, offering both high efficiency and strong physical interpretability:

1) The proposed model was validated against FEM simulations under various velocity conditions. The maximum deviation between the analytical and FEM results was 4.06% at 5 m/s, demonstrating strong consistency and confirming the reliability of the model.
2) The model accurately captures the effects of multi-DOF motion, including vertical and horizontal displacements as well as pitch, roll, and yaw angle variations. The analytical results closely match FEM simulations, with maximum discrepancies typically within 3.2%.
3) A full-scale PMLB prototype and precision measurement platform was developed to assess braking performance. Tests conducted at three different speeds measured both induced eddy currents and transient braking forces. The maximum deviation between experimental data and analytical predictions was 6.7%.

REFERENCES

[1] S. Mohammadi and M. Mirsalim, "Double-sided permanent-magnet radial-flux eddy-current couplers: three-dimensional analytical modelling, static and transient study, and sensitivity analysis," *IET Electr. Power Appl.*, vol. 7, no. 9, pp. 665-679, Nov. 2013.

[2] B. Kou, H. Zhang, X. Yin, Y. Zhou and C. Li, "Research on long stroke moving secondary permanent magnet linear eddy current braking," *CES Transactions on Electrical Machines and Systems*, vol. 3, no. 1, pp. 19-29, Mar. 2019.

[3] H. Shi, T. Cao, H. Yi, X. Zhou, S. Jiang and Z. Deng, "Exploration of Split-Guideway Permanent Magnet Linear Eddy Current Braking With Improved Braking Force and Critical Speed Implemented in HTS Maglev System," *IEEE Trans. Transport. Electrific*., vol. 10, no. 2, pp. 4201-4216, June. 2024.

[4] Z. Li, Y. Li, B. Qu, H. Yang, X. Zhu and D. Wang, "Evaluation and Analysis of Flux-Regulated Permanent Magnet Linear Eddy Current Brakings," *IEEE Trans. Ind. Appl.*, vol. 59, no. 1, pp. 712-725, Feb. 2023.

[5] D. Valderas, I. Mesa, I. Adín, H. Lehmann, G. Lancaster, and O. Stark, "Modeling eddy current braking emissions for electromagnetic compatibility with signaling devices in high-speed railways," *IEEE Trans. Veh. Technol.*, vol. 66, no. 11, pp. 9743–9752, Nov. 2017.

[6] A. Canova and B. Vusini, "Analytical modeling of rotating eddy-current couplers," *IEEE Trans. Magn.*, vol. 41, no. 1, pp. 24–35, Jan. 2005.

[7] B. Zhang, T. Peng, Q. Chen, and Q. Cao, "3-D nonlinear transient analysis and design of eddy current braking for high-speed trains," *Int. J. Appl. Electromagn. Mech.*, vol. 40, no. 3, pp. 205–214, Jan. 2012.

[8] S. Cho, H. Liu, H. Ahn, J. Lee, and H. Lee, "Eddy current braking with a two-layer structure: Calculation and characterization of braking performance," *IEEE Trans. Magn.*, vol. 53, no. 11, pp. 1–5, Nov. 2017.

[9] B. Kou, W. Chen and Y. Jin, "A Novel Cage-Secondary Permanent Magnet Linear Eddy Current Braking With Wide Speed Range and its Analytical Model," *IEEE Trans. Ind. Electron*., vol. 69, no. 7, pp. 7130-7139, July. 2022.

[10] M. Wang, L. Zhang, K. Yang, J. Xu, and C. Du, "Eddy Current Braking Force Analysis of a Water-Cooled Ironless Linear Permanent Magnet Synchronous Motor," *Energies*, vol. 16, no. 15, pp. 1-16, Aug. 2023.

[11] M. Hecquet, P. Brochet, Lee Sang Jin and P. Delsalle, "A linear eddy current braking system defined by finite element method," *IEEE Trans. Magn.*, vol. 35, no. 3, pp. 1841-1844, May. 1999.

[12] T. W. Nehl, B. Lequesne, V. Gangla, S. A. Gutkowski, M. J. Robinson and T. Sebastian, "Nonlinear two-dimensional finite element modeling of permanent magnet eddy current couplings and brakings," *IEEE Trans. Magn.*, vol. 30, no. 5, pp. 3000-3003, Sept. 1994.

[13] M. Fujita, T. Tokumasu, T. Yamada, T. Hirose, Y. Tanaka, N. Kumagai, and S. Uchida, "3-dimensional electromagnetic analysis and design of an eddy-current rail braking system," *IEEE Trans. Magn.*, vol. 34, no. 5, pp. 3548–3551, Sep. 1998.

[14] J. Li, Y. Li, J. Xu, J. Luo, S. Xu, Y. Li, M. Zeng, H. Yu. L. Cui, X. Song, and G. Ma, "Calculation and Characterization of Braking Performance for Rail Eddy Current Braking With AC Excited Ring-Winding Armature," *IEEE Trans. Ind. Appl.*, vol. 59, no. 2, pp. 1614-1625, Mar. 2023.

[15] H. J. Shin, J. Y. Choi, H. W. Cho and S. M. Jang, "Analytical Torque Calculations and Experimental Testing of Permanent Magnet Axial Eddy Current Braking," *IEEE Trans. Magn.*, vol. 49, no. 7, pp. 4152-4155, July. 2013.

[16] Y. Oner, Z. Q. Zhu, L. J. Wu, X. Ge, H. Zhan, and J. T. Chen, "Analytical on-load subdomain field model of permanent-magnet vernier machines," *IEEE Trans. Ind. Electron.*, vol. 63, no. 7, pp. 4105–4117, Jul. 2016.

[17] X. Niu, B. Kou, H. Zhang, C. Huang and L. Zhang, "Modeling and Analysis of Rail Eddy Current Braking With Ring Structure Winding and AC Excitation," *IEEE Trans. Ind. Electron.*, vol. 71, no. 11, pp. 13590-13600, Nov. 2024.

[18] Y. Jin, B. Kou and L. Li, "Improved Analytical Modeling of an Axial Flux Double-Sided Eddy-Current Braking With Slotted Conductor Disk," *IEEE Trans. Ind. Electron.*, vol. 69, no. 12, pp. 13277-13286, Dec. 2022.

[19] M. Gulec, P. Lindh, M. Aydin and J. Pyrhönen, "Cost Minimization of a Permanent Magnet Eddy Current Braking by Multiobjective Particle Swarm Optimization Based on Nonlinear Reluctance Network Modeling," *IEEE Access.*, vol. 9, pp. 157361-157370, Nov. 2021.

[20] A. J. Mäkinen, R. Zetter, J. Iivanainen, K. C. J. Zevenhoven, L. Parkkonen, and R. J. Ilmoniemi, "Magnetic-field modeling with surface currents. Part I. Physical and computational principles of bfieldtools," *J. Appl. Phys.*, vol. 128, no. 6, pp. 1-16, Aug. 2020.

[21] Z. Su, J. Luo, G. Ma, K. Liu, L. Cui and Y. Wang, "Fast and Precise Calculation of Mutual Inductance for Electrodynamic Suspension: Methodology and Validation," *IEEE Trans. Ind. Electron.*, vol. 69, no. 6, pp. 6046-6057, June 2022.

[22] L. Cui, G. Ma, J. Luo, Z. Su and P. Feng, "Theoretical Modelling of Permanent Magnet Linear Eddy Current Brake Based on Equivalent Circuit," *2025 15th International Symposium on Linear Drivers for Industry Applications (LDIA)*, Daejeon, Korea, pp. 1-4, 2025.

[23] J. Choi, H. Lee, S. Yoo and M. D. Noh, "Analysis and Modeling of a Voice-Coil Linear Vibration Motor Using the Method of Images," *IEEE Trans. Magn.*, vol. 48, no. 11, pp. 4164-4167, Nov. 2012.

[24] L. Chen, J. Wang and S. S. Nair, "An Analytical Method for Predicting 3-D Eddy Current Loss in Permanent Magnet Machines Based on Generalized Image Theory," *IEEE Trans. Magn.*, vol. 52, no. 6, pp. 1-11, June 2016, Art no. 8103311.

[25] Z. Su, G. Ma and J. Luo, "Analytical Modeling of the Closed-Loop Operation and Quench Behavior for Superconducting Electrodynamic Suspension Train," *IEEE Trans. Transp. Electrific.*, vol. 8, no. 1, pp. 1026-1039, March 2022.

Libin Cui received the B.E. degree in vehicle engineering and M.E. degree in traffic and transportation from Southwest Jiaotong University, Chengdu, China, in 2020 and 2023, respectively. He is currently working toward a Ph.D. degree in vehicle operation engineering with Southwest Jiaotong University, Chengdu, China. His current research interests include electrodynamic suspension and linear motor.

Guangtong Ma (Senior Member, IEEE) received the B.E. and Ph.D. degrees in electrical engineering from Southwest Jiaotong University (SWJTU), Chengdu, China, in 2005 and 2009, respectively. From 2011 to 2013, he was an Alexander von Humboldt Research Fellow with Technische Universität Darmstadt, Darmstadt, Germany. From 2010 to 2023, he was with the State Key Laboratory of Rail Transit Vehicle System, SWJTU, where he was a full professor and deputy director. Since 2024, he has been with the dean of the School of Electrical Engineering, SWJTU. His research interests include superconducting suspension, linear motor and traction motor.

Pedram Asef (Senior Member, IEEE) received the Ph.D. degree (cum laude) in electrical engineering from the Polytechnic University of Catalonia (UPC), Barcelona, Spain, in 2019. He is currently an Assistant Professor with the Department of Mechanical Engineering, University College London (UCL). He is the Director of the e-Motion Laboratory and a member of the Advanced Propulsion Laboratory with UCL. He published over 60 peer reviewed papers and two books. He led related funded research and industrial projects worth more than £ six million in the past years. His research interests include electrical machines and drives, power systems, electric vehicles, and applied optimization and machine learning methods.

Zhenhua Su received the B.E. and M.E. degrees in vehicle engineering from Chongqing Jiaotong University, Chongqing, China, in 2017 and 2020, respectively. He received the Ph.D. degree in vehicle operation engineering from Southwest Jiaotong University, Chengdu, China, in 2024. From 2023 to 2024. he was a special Research Student with the University of Tokoy, Kashiwa, Japan. Since 2024, he has been with the School of Electrical Engineering, Southwest Jiaotong University, Chengdu, China, where he is currently a Post-Doctoral Fellow. His current research interests include vehicle dynamics, electrodynamic suspension and linear motor.

Piji Feng received the B.E. degree in mechanical engineering from Southwest Jiaotong University, Chengdu, China, in 2019. He is currently working toward the Ph.D. degree in vehicle operation engineering with Southwest Jiaotong University, Chengdu, China. His current research interests include electrodynamic suspension, vehicle dynamics and vibration control.

Guanglai Huang received the B.E. degree in mechanical design, manufacturing and automation from Southwest Jiaotong University, Chengdu, China, in 2022. He is currently working toward a Ph.D. degree in vehicle operation engineering with Southwest Jiaotong University, Chengdu, China. His current research interests include the axial-flux permanent magnet synchronous motor

Shuai Xu (Member, IEEE) received the B.Sc. and M.Sc. degrees in electrical engineering from Henan Polytechnic University, Jiaozuo, China, in 2011 and 2013, respectively, and the Ph.D. degree in electrical engineering from Southeast University, Nanjing, China, in 2018.

From 2016 to 2017, He was a joint Ph.D. student with University of British Columbia, Vancouver, Canada. Since 2019, he has been with the State Key Laboratory of Rail Transit Vehicle System, Southwest Jiaotong University, Chengdu, China. His research interests include multilevel converters, motor drives, fault diagnosis and fault-tolerant control.

Jun Luo (Member, IEEE) received the B.E., M.E., and Ph.D. degrees in electrical engineering from the Harbin Institute of Technology (HIT), Harbin, China, in 2012, 2014, and 2020, respectively. Since 2020, he has been with the State Key Laboratory of Rail Transit Vehicle System at Southwest Jiaotong University, Chengdu, China, where he is currently an Associate Researcher. His research focuses on the analysis and design of linear motors, electrodynamic suspension systems, and superconducting direct-drive motors.